Photoresistive gas sensor based on nanocrystalline ZnO sensitized with colloidal perovskite $CsPbBr_3$ nanocrystals

Photoresistive gas sensor based on nanocrystalline ZnO sensitized with colloidal perovskite $CsPbBr_3$ nanocrystals

A.S. Chizhov [a,*], M.N. Rumyantseva [a,b], K.A. Drozdov [c], I.V. Krylov [c], M. Batuk [d], J. Hadermann [d], D.G. Filatova [a], N.O. Khmelevsky [e], V.F. Kozlovsky [a], L.N. Maltseva [a], A.M. Gaskov [a,b]

[a] *Chemistry Department, Moscow State University, Moscow, 119991, Russia*
[b] *Saint Petersburg State University, Petergof, 198504, Saint Petersburg, Russia*
[c] *Faculty of Physics, Moscow State University, Moscow, 119991, Russia*
[d] *EMAT, University of Antwerp, B-2020, Antwerp, Belgium*
[e] *LISM, Moscow State Technological University Stankin, 127055, Moscow, Russia*

A B S T R A C T

The development of sensor materials of which gas sensitivity activates under light illumination is of great importance for the design of portable gas analyzers with low power consumption. In the present work a ZnO/ $CsPbBr_3$ nanocomposite based on nanocrystalline ZnO and colloidal cubic-shaped perovskite $CsPbBr_3$ nano-crystals (NCs) capped by oleic acide and oleylamine was synthesized. The individual materials and obtained nanocomposite are characterized by x-ray diffraction, low-temperature nitrogen adsorption, x-ray photoelectron spectroscopy, high angle annular dark field scanning transmission electron microscopy with energy-dispersive X- ray spectroscopy mapping and UV–vis absorption spectroscopy. The spectral dependence of the photoconductivity of the ZnO/$CsPbBr_3$ nanocomposite reveals a well-defined peak that strongly correlates with the its optical absorption spectrum. The nanocomposite ZnO/$CsPbBr_3$ shows enhanced photoresponse under visible light illumination ($\lambda_{max} = 470$ nm, 8 mW/cm^2) in air, oxygen and argone, compared with pure nanocrystalline ZnO. Under periodic illumination in the temperature range of 25– 100 °C, the ZnO/$CsPbBr_3$ nanocomposite shows a sensor response to 0.5–3.0 ppm NO_2, unlike pure nanocrystalline ZnO matrix, which demonstrates sensor sensitivity to NO_2 under the same conditions above 100 °C. The effects of humidity on the sensor signal and photoresponse are also discussed.

1. Introduction

Detection of toxic and explosive gases in the atmosphere is of great importance for ensuring the safety of people both at work and in everyday life. Reliable detection of such gases in air is a complex task due to the chemical diversity of toxic gases, their extremely low allowable concentration (sometimes below 1 ppm) and the continuously changing environmental conditions (temperature, humidity, atmospheric composition fluctuations). One promising type of gas sensor is based on a reversible change in the electrical resistance of the semiconductor metal oxide layer upon changes in the composition of the atmosphere [1,2]. Such resistive gas sensors show a high sensitivity to various gases, are cheap, have a simple construction and a small size. Selectivity can be provided by modifying the surface of the metal oxide layer with various catalytic additives (particles of transition metal oxides, clusters of noble metals) [3,4]. Such catalytic additives promote a certain type of chemical reactions on the surface of the sensor, affecting the electrical conductivity of the metal oxide layer. The main disadvantage of resistive gas sensors, which prevents their use in mobile and portable devices, is the need to heat the sensitive metal oxide layer to a high temperature (150 −500 °C), which entails increased power consumption [5,6].

A number of studies performed on metal oxide sensors showed that gas sensitivity can be activated by exposure to ultraviolet (UV) radiation at room temperature without additional heating [7–11]. This is a promising way for reducing the power consumption of the gas sensors, since low-power light sources, such as light-emission diodes (LEDs), can be used for irradiation. The gas sensitivity of nanocrystalline wide-gap metal oxide layers is also activated by visible-light irradiation, but the effect is not pronounced, since it is affected by light absorption due to

* Corresponding author.
E-mail address: chizhov@inorg.chem.msu.ru (A.S. Chizhov).

impurities or defects in the crystal structure of semiconductor particles [12–14]. To enhance the sensitivity of sensor materials to visible light, wide-gap metal oxides can be combined with substances that strongly absorb visible light (sensitizers), such as dyes [15–17], plasmon [18–24] and non-plasmonic [25] metal nanoparticles, narrow-band semiconductor nanoparticles [26–28], carbon nanomaterials [29–32] and semiconductor quantum dots [33–37]. By this sensitization approach, the absorption spectrum of the sensor layer can be matched to the emission spectrum of the light source, which allows to optimize the efficiency of excitation energy transfer from the light source to the sensor layer and shift the absorption edge to lower radiation energy.

Colloidal lead halide nanocrystals (NCs) $APbX_3$ (where $A = CH_3NH_3^+$ (MA), $(NH_2)_2CH^+$ (FA), Cs^+ and $X = Cl^-$, Br^- , I^-) crystallizing in the perovskite structure have received a lot of attention in recent years due to their unique optical properties, such as strong light absorption, high quantum yield of photoluminescence (up to 99+%) and narrow-edge photoluminescence (PL) peaks, the possibility to tune their optical properties within the entire visible range, mainly by changing their anion composition, and their facile synthesis possible under ambient conditions [38–40]. Unlike traditional semiconductor quantum dots, such as CdSe or InP, nonradiative recombination of photoexcited electron-hole pairs in pure $CsPbBr_3$ NCs is almost suppressed [41], which, in combination with the high position of the excited energy level, creates favorable conditions for effective injection of photoexcited charge carriers into the conduction band of wide-gap metal oxides. These properties make colloidal lead halide perovskites promising candidates for sensitizing wide-gap metal oxides to visible light.

Currently, there are only few studies of lead halide perovskite NCs for light-activated gas sensor applications. Chen and co-workers developed the self-powered gas sensors based on a polycrystalline $CsPbBr_3$/FTO (fluorine-doped tin oxide layer) [42] and $CsPbBr_2I/TiO_2$/FTO [43] structures demonstrated a high sensor response to oxygen, acetone, ethanol and NO_2 at room temperature and utilized visible light (solar) illumination. The work [44] revealed the gas sensitivity of the $MAPbI_3/SnO_2$/Au composite structure to NO_2 at room temperature and radiation of a Xe lamp. Methylammonium tin iodide was used as an efficient light harvester, however, it is well known that tin-based perovskites have poor chemical and environmental stability due to the ease of oxidation of Sn^{2+} to Sn^{4+} [40]. At the same time, a number of recent works [45–54] were devoted to the investigation of organometallic halide perovskites, but the authors did not study the effect of light on the sensor properties. The work [55] noted a high sensitivity to ozone of the sensor based on $CsPbBr_3$ ligand-free nanocubes at room temperature. Thus, although the optical absorption of the metal perovskite halides covers the entire visible range, a systematic study of their influence on the photoconductivity and the gas sensitivity of wide-gap semiconductor oxides under visible light illumination has not yet been carried out.

Since the replacement of thermal heating by light irradiation primarily intends to reduce the energy consumption of resistive gas sensors, it is necessary to take into account the energy expended on the illumination, which also depends on the quantum efficiency of the applied miniature light sources. The greatest external quantum efficiency is currently provided by InGaN/GaN LEDs with the maximum radiation in the blue range, while green and yellow LEDs show a dramatic drop in their efficiency [56], therefore their use is not profitable in terms of saving energy. Ultraviolet LEDs are also currently of low efficiency and the technology of their manufacture remains expensive and imperfect [57]. Thereby, the most preferred range is blue light (420−480 nm), which coincides with the absorption edge of colloidal perovskite bromides. We also note that fully all-inorganic perovskites show greater stability than those containing organic cations [40].

This work reports the study of the photoconductivity and visible-light activated gas sensor properties of nanocrystalline ZnO sensitized with colloidal $CsPbBr_3$ nanocrystals.

2. Experimental methods

2.1. Synthesis of materials

Nanocrystalline ZnO powder was prepared by reaction of equimolar amounts of zinc acetate and ammonium bicarbonate in aqueous medium at 20 °C. 0.893 M solution of $Zn(CH_3COO)_2{*}2H_2O$ was slowly added to 1.5 M solution of NH_4HCO_3 under vigorous stirring. The resulting white precipitate of basic zinc carbonate $Zn_x(OH)_y(CO_3)_z$ was filtered under vacuum, washed several times with water and ethanol and dried at 70 °C. To form nanocrystalline ZnO, the precipitate was annealed at 300 °C in air for 24 h.

The colloidal perovskite $CsPbBr_3$ NCs were synthesized by hot-injection method using the Schlenk line according to Protesescu et al. [38] with only small differences (a detailed description of the synthesis is given in the Supplementary information).

To study the photoconductance and gas sensor properties, the ZnO/$CsPbBr_3$ nanocomposite was formed directly on a dielectric (Al_2O_3) plate with dimensions of 1.5 × 1.5 mm (Fig. 1a), equipped with Pt measuring contacts and a Pt helix on the back of the plate, allowing to heat up the nanocomposite layer. Manufacturing of the ZnO/$CsPbBr_3$ nanocomposite layer consisted of several steps: (i) nanocrystalline ZnO powder was mixed with α-terpeniol to form a thick paste, which was transferred to the measuring plate; (ii) the applied ZnO-based paste layer was slowly dried at 50 °C and then sintered at 350 °C in air for 24 h to form the ZnO layer of 50−100 μm thickness (Fig. 1b); (iii) 2−4 μl of hexane sol of $CsPbBr_3$ NCs was dropped on the obtained ZnO layer, then the nanocomposite ZnO/$CsPbBr_3$ layer was dried at 70 °C in air for 12 h.

2.2. Materials characterization

Phase composition and crystal structure of synthesized materials was studied by powder X-ray diffraction (XRD) with a Rigaku diffractometer

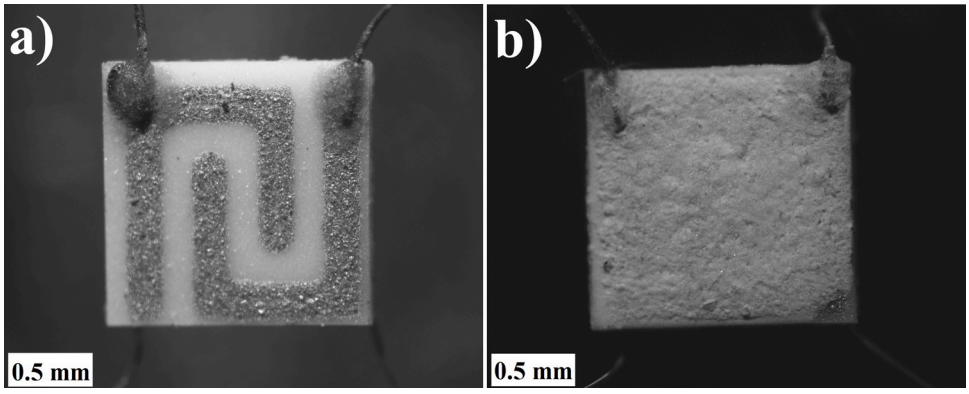

Fig. 1. (a) Measuring plate with Pt electrodes; (b) Metal-oxide layer applied on the measuring chip.

using CuKα radiation (wavelength λ = 1.54059 Å). The specific surface area of nanocrystalline ZnO was measured by low-temperature nitrogen adsorption using the BET model with the Chemisorb 2750 instrument (Micromimetics).

Investigation of the shape and size of the nanocrystals and the microstructure of the ZnO/$CsPbBr_3$ nanocomposite was performed by high-angle annular dark field scanning transmission electron microscopy (HAADF-STEM) and energy dispersive X-ray spectroscopy (EDX) maps acquired using a FEI Osiris microscope equipped with a Super-X detector and operated at 200 kV. To prepare the samples for analysis, the material was mixed with toluene using an ultrasonic bath. A few drops of the obtained suspension were deposited onto a Cu TEM grid covered with carbon.

For the spatial distribution examination and sensor surface mapping, high resolution μ-XRF spectrometer M4 Tornado Plus (Bruker Nano GmbH, Germany) was used. Following lines were used: Cs, Pb, L_3-M_5, Br, Zn – K-L_3.

The absorption spectra of colloidal NCs were recorded on a Varian Cary 50 spectrophotometer in the range of 300− 1100 nm. The PL spectra were registered using the USB-4000 spectrometer («Ocean Optics»). Absorption spectrum of ZnO/$CsPbBr_3$ nanocomposite in the wavelength range of 300–800 nm was recorded using Perkin–Elmer Lambda 35 spectrometer.

X-ray photoelectron spectroscopy (XPS) measurements were performed using a K-Alpha (Thermo Scientific) spectrometer with an Al Kα X-ray source (E =1486.7 eV). The sample was prepared by dropping a sol of $CsPbBr_3$ NCs in hexane onto a Si plate. The charge correction was performed relative to the main carbon C1s peak, the binding energy of which was assumed to be 285 eV.

The spectral dependence of the photoconductivity was studied in the range of 390− 700 nm. The radiation from a 100 W white light source was passed through an MDR-206 monochromator. The conductivity of the samples was measured on a Keithley 6517 instrument. The measurements were carried out in ambient air at room temperature. The photoconductivity

$$\sigma_{ph} = \frac{\sigma_\lambda - \sigma_0}{\sigma_0} \quad (1)$$

where σ_λ is the photoconductivity value at wavelength λ and σ_0 is the conductivity of the sample in the dark.

The weight content of $CsPbBr_3$ NCs in the nanocomposite was determined by inductively coupled plasma mass spectrometry (ICP-MS) on a quadrupole ICP mass spectrometer (Agilent 7500c; Agilent Technologies, Waldbronn, Germany). The nanocomposite layer was washed with two portions (2 mL) of 10 % nitric acid and then the sample was diluted with water to 10.00 mL. Analytical signals were measured and data were processed using the built-in ChemStation software (G1834B version). Measurements were performed for isotopes $^{64,68}Zn$, $^{79,81}Br$, ^{133}Cs and ^{206}Pb.

The sensor measurements were carried out in a 50-ml opaque flow cell. The temperature of sensors during the gas sensing measurements was maintained with an accuracy of ±2 °C.The resulting NO_2 gas concentration was obtained by mixing the standard gas mixture (100 ± 1 ppm NO_2 in nitrogen) and the synthetic dry air using Bronkhorst mass-flow controllers. The air humidity was set by passing dry air through a bubbler with distilled water. During the measurements, the gas flow through the cell was maintained at 100 mL/min. The blue LED used for sensor measurements had a maximum of emitted light at 470 nm (the emission spectrum of the LED is presented in the Supplementary information, Fig. S1); the irradiance was 8 mW/cm^2 at the plane where the sensors were placed. For periodic illumination, a cyclic time relay was used to interrupt the LED power supply circuit at certain time intervals.

3. Results and discussion

3.1. Characterization of samples

3.1.1. Nanocrystalline ZnO

According to XRD analysis, the decomposition of zinc hydroxide

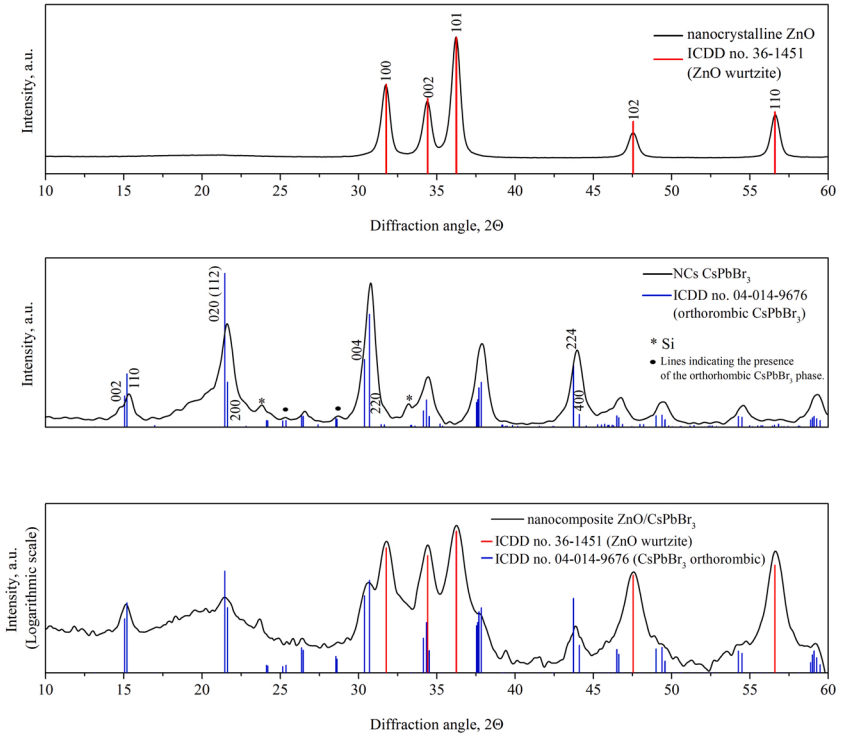

Fig. 2. X-ray diffraction patterns for nanocrystalline ZnO (a), colloidal $CsPbBr_3$ NCs (b) and ZnO/$CsPbBr_3$ nanocomposite (c).

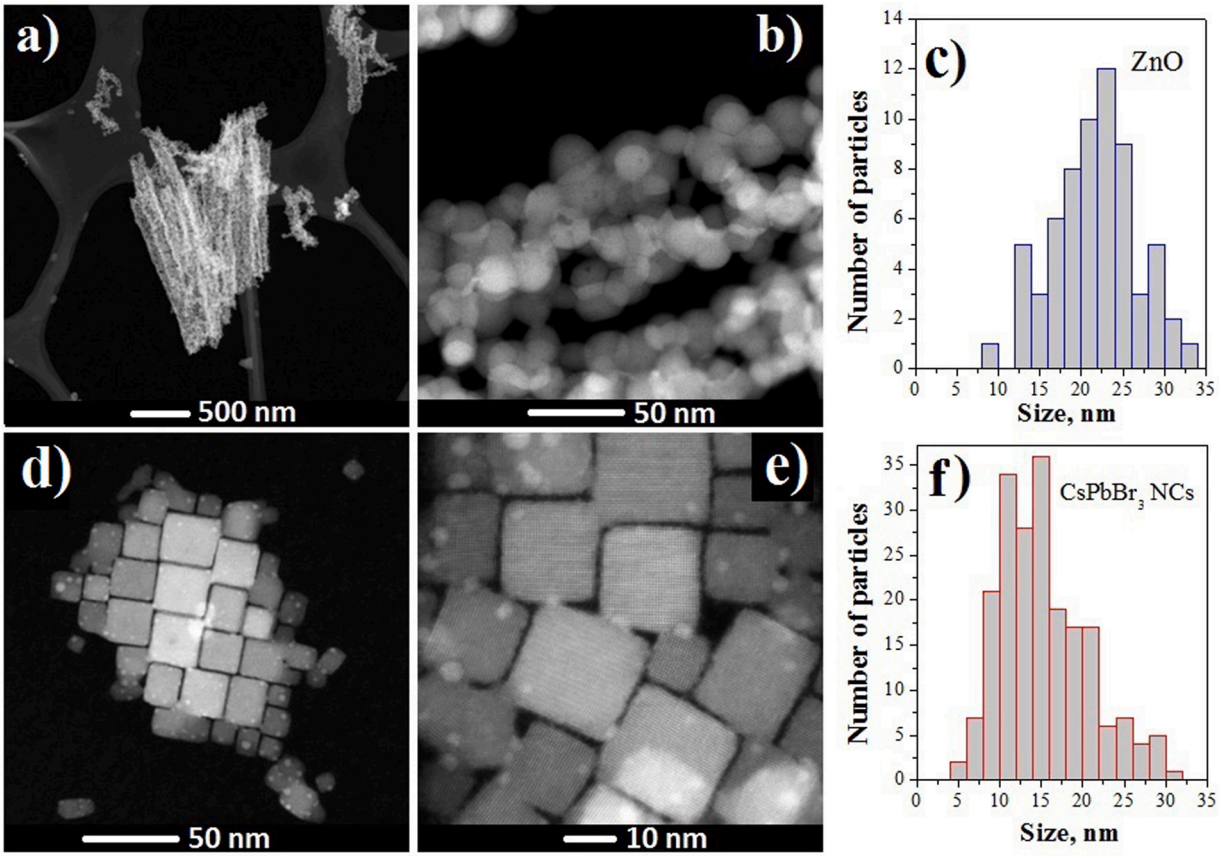

Fig. 3. a,b) HAADF-STEM images of nanocrystalline ZnO aggregates at different magnifications and c) the ZnO particles size distribution; d,e) HAADF-STEM images of $CsPbBr_3$ NCs at different magnifications and f) the $CsPbBr_3$ particles size distribution.

carbonates at 300 °C leads to the pure ZnO wurtzite phase with lattice parametres $a = 3.24980(17)$ and $c = 5.20518(18)$Å (Fig. 2a). The average size of the ZnO crystallites, calculated from the Scherrer equation, lies in the range of 12−15 nm. The ZnO crystallites are typically combined to larger rod-like aggregates of about 100 nm in diameter and several μm in length (Fig. 3a). The average crystallite size, measured from HAADF-STEM images, is 22 ± 5 nm, with a crystal shape close to spherical (Fig. 3b,c). The specific surface area of the nanocrystalline ZnO powder is 40 ± 2 m^2/g.

3.1.2. *Colloidal $CsPbBr_3$ NCs*

An X-ray diffraction pattern of synthesized colloidal $CsPbBr_3$ NCs is shown in Fig. 2b. The crystal structure of the colloidal $CsPbBr_3$ NCs has been studied in a few works [58,59], however, the question whether the structure is orthorhombic or cubic remains controversial. From the routine X-ray phase analysis data, it is difficult to establish the crystal structure of colloidal NCs due to the broadening of the diffraction peaks. The presence of the reflections at 2θ = 25.2° and 28.2° indicates that the structure is orthorhombic (space group *Pnma*), since these reflections are absent for the cubic one (space group *Pm-3 m*) (Supplementary Information, Fig. S2). The $CsPbBr_3$ NCs have a shape close to cubic (rectangular cuboids), as can be seen from the HAADF-STEM images (Fig. 3d,e), and have a broad particle size distribution with the average size of 15 ± 6 nm (Fig. 3f). The nanocubes are randomly covered with small spherical particles with a size of 2−5 nm, which according to STEM-EDX maps are Pb or PbO (Supplementary information, Figs. S3 and S4). The photoluminescence of the $CsPbBr_3$ NCs sol in hexane shows one peak with λ_{max} = 515 nm and FWHM = 20 nm (Fig. 4a). The optical band gap of $CsPbBr_3$ NCs, calculated from the sol absorption spectrum is 2.39 eV for direct allowed transitions (Fig. 4b). The charge state of the Cs, Pb and Br atoms in $CsPbBr_3$ NCs has been determined by XPS

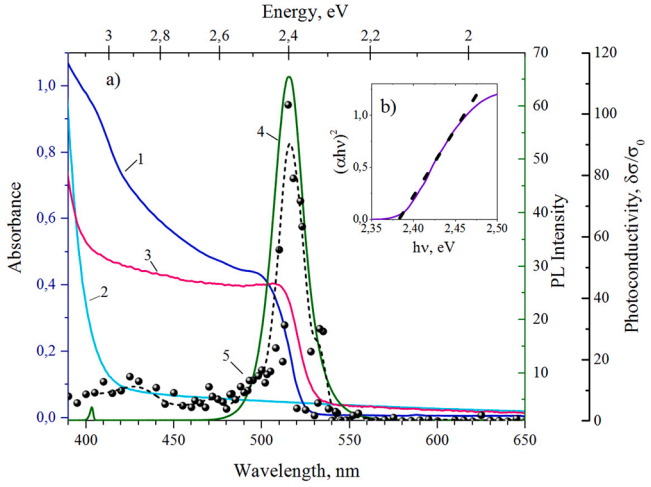

Fig. 4. a) Optical absorption spectra of colloidal $CsPbBr_3$ NCs in hexane (1), nanocrystalline ZnO (2) and ZnO/$CsPbBr_3$ nanocomposite (3); photoluminescence spectrum of colloidal $CsPbBr_3$ NCs in hexane (4); photoconductivity spectrum of ZnO/$CsPbBr_3$ nanocomposite (5); b) Determination E_g of $CsPbBr_3$ NCs from optical absorption using a Tauc plot.

analysis. The Pb4f spectrum is represented by two doublets with a difference in the binding energy of 1.4 eV and the intensity ratio about 1:100 (Fig.5a). The most intense component Pb4f(I) corresponds to the Pb^{2+} oxidation state, the other component Pb4f(II) has a binding energy of 136.9 eV which is close to metallic Pb. The presence of metallic lead in lead halide perovskites analyzed by XPS was noted in other studies

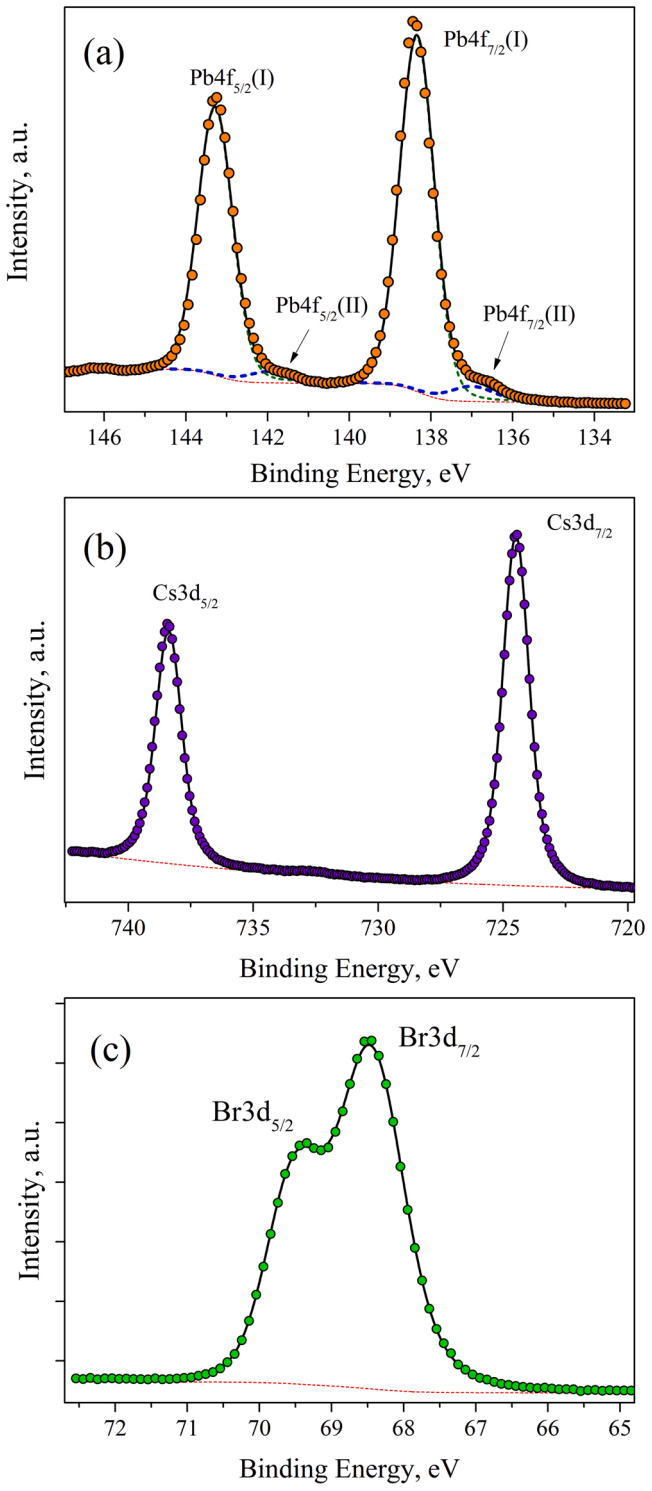

Fig. 5. XP spectra of $CsPbBr_3$ NCs on the Pb4f (a), Cs3d (b) and Br3d (c) regions.

and may be a consequence of both photolysis of the sample under the x-ray radiation and aging of the sample in air [60]. The position of the Br3d and Cs3d doublets corresponds to the single charge state of Br^- and Cs^+, respectively (Fig. 5b,c). In addition, the O1s and N1s peaks are observed in the XP spectra of the sample, which may be due to the presence of these atoms in the capping ligands oleic acid and oleylamine (see Supplementary information, Fig. S5). Analysis of the crude $CsPbBr_3$ NCs by ICP-MS showed an excess of lead and bromine, with an element ratio Cs:Pb:Br = 1.00 : 1.13 : 4.00. A close to stoichiometric composition $CsPbBr_{3.06}$ was obtained after washing the nanocrystals three times with ethyl acetate (See Supplementary Information for details).

3.1.3. *ZnO/$CsPbBr_3$ nanocomposite*

The HAADF-STEM analysis of $CsPbBr_3$ particles in the ZnO/$CsPbBr_3$ nanocomposite is hampered by the presence of ZnO aggregates. Nevertheless, several areas containing $CsPbBr_3$ particles were found and their examples are shown in Fig. 6 (see also Supplementary Information, Figs. S6 and S7). According to the images, the cubic morphology of $CsPbBr_3$ is not preserved in the composite, that can be caused by the typical process of sample preparation for electron microscopy (dispersion of the nanocomposite in toluene under the ultrasonic treatment). The detected $CsPbBr_3$ nanoparticles have different shapes and sizes, equal to or slightly larger than the size of the original $CsPbBr_3$ nanocubes. No huge regions of Cs were found on the elemental maps of the distribution of Zn and Cs elements over the surface of the sensor, which indicates the absence of significant agglomeration of $CsPbBr_3$ NCs during the formation of nanocomposites (Fig. S8). In the optical spectrum of the ZnO/$CsPbBr_3$ nanocomposite, the absorption edge of $CsPbBr_3$ NCs undergoes a red shift of 7−8 nm relative to the spectrum of $CsPbBr_3$ NCs hexane sol (Fig. 4a). The obtained XRD pattern for the ZnO/$CsPbBr_3$ nanocomposite shows the lines of both nanocrystalline ZnO and perovskite nanocrystals, which confirms that the crystalline $CsPbBr_3$ phase is retained (Fig. 2c). It seems that the formation of a nanocomposite changes the morphology of $CsPbBr_3$ NCs, but not their crystal structure. In general, the content of $CsPbBr_3$ NCs in the ZnO/$CsPbBr_3$ nanocomposite was about 7.5 % based on the ICP-MS measurements.

3.2. *Spectral dependence of photoconductivity*

The photoconductivity spectrum of ZnO/$CsPbBr_3$ nanocomposite is shown in Fig. 4a. Compared with the earlier studied photoconductivity spectra of metal oxide nanocomposites sensitized with semiconductor colloidal QDs [33–36,61–63], the spectrum presented in Fig. 4a has following noteworthy features: (i) a well-defined narrow photoconductivity peak is observed that correlates with the position of the absorption edge of ZnO/$CsPbBr_3$ nanocomposite; (ii) extremely high σ_{ph} values (up to 100) were obtained for ZnO/$CsPbBr_3$ nanocomposite, while under similar experimental conditions, ZnO-based nanocomposites sensitized with CdSe and InP QDs showed significantly lower values (up to 0.3 and 0.017, respectively).

It is interesting to note that the maximum photoconductivity among the different nanocomposites (σ_{ph}) correlates with the calculated Gibbs free energy (ΔG^o_{ET}) as a result of photoinduced electron transfer. According to [64], the ΔG^o_{ET} takes into account three contributions related to the position of donor and acceptor levels (ΔG_{electr}), the energy needed on the spatial separation of the electron and hole ($\Delta G_{coloumb}$) and the difference associated with having non-neutral donating and accepting species following the electron transfer ($\Delta G_{charging}$):

$$\Delta G^o_{ET} = \Delta G_{electr} + \Delta G_{coloumb} + \Delta G_{charging} \quad (2)$$

Based on the Markus model [65], a relationship can be established between the ΔG^o_{ET} and the rate constant of electron transfer k_{ET}. The calculated values are shown in the Table 1. The data required for the calculation and the method of calculation are given in the Supplementary Information.

3.3. *Oxygen-controlled photoconductivity*

Nanocomposite materials based on the nanocrystalline metal oxides have long relaxation times ($>10^3$ min) of the photoconductivity [61–63], which hampers sensor measurements in equilibrium conditions. However, the investigation of gas sensitivity under light illumination can be carried out in stationary conditions that do not require establishing electrical conductivity values. Turning periodically the

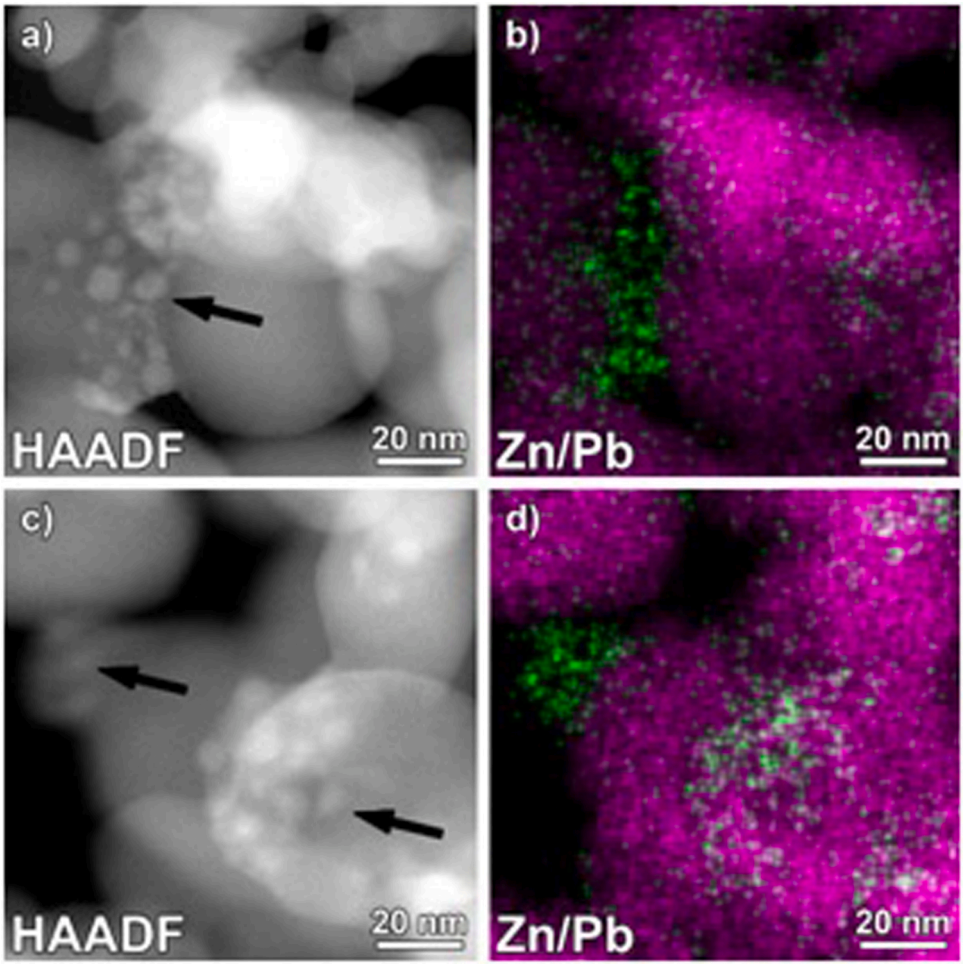

Fig. 6. Complementary HAADF-STEM images and elemental maps from two different areas (a,b and c,d) of ZnO/$CsPbBr_3$ nanocomposite containing $CsPbBr_3$ (shown by arrows). On the mixed maps, only Zn (pink) and Pb (green) maps are overlapped for clarity. STEM-EDX maps of other elements are shown in the Supplementary Information, Figs. S6 and S7. (For interpretation of the references to colour in the Figure, the reader is referred to the web version of this article).

Table 1
Maximum photoconductivity σ_{ph} of three ZnO-based nanocomposites sensitized with quantum dots, calculated values of ΔG_{ET} and evaluated values k_{ET} according model from [48].

	ZnO/QD_InP (4 nm) [28]	ZnO/QD_CdSe (2.8 nm) [26]	ZnO/$CsPbBr_3$(15 nm) (this work)
σ_{ph}, max	0.17	0.3	100
ΔG^{o}_{ET}, eV	−0.02	−0.38	−0.93
k_{ET}, 10^{10} s^{-1}	~5	~20	~30

light source on and off at regular intervals t_{light} and t_{dark}, the observed graph σ(t) will show the alternating increase and decay of photoconductivity [66,67]. In this way, the atmosphere effect on the photoconductivity is determined by kinetics of light-induced effects, such as photoadsorption, photodesorption, photocatalytic processes and relaxation of photogenerated carriers.

Fig. 7a presents the photoconductivity change of ZnO/$CsPbBr_3$ nanocomposite compared to non-sensitized nanocrystalline ZnO sensor under periodical blue LED illumination (t_{light}=t_{dark} = *2 min*) in dry air, Ar and O_2 atmosphere. On the air, the photoconductivity for both samples sharply increases compared to the dark conductivity: by about 10^3 for nanocomposite and about 10^2 for pure ZnO. Thus, the sensitizing effect of $CsPbBr_3$ NCs on the photoconductivity of ZnO under visible light irradiation is clear. After several cycles of illumination, the steady state is established, which is characterized by nearly equal values G_{light} and G_{dark} at the end of each period t_{light} and t_{dark} but for ZnO steady state is achieved slower and a constant drift of the photoconductivity is observed. A photoresponse under periodic illumination can be defined as the ratio of G_{light} to G_{dark}:

$$\Phi = \frac{G_{light}}{G_{dark}} \quad (3)$$

On the Fig. 7a it is clearly seen that the ZnO/$CsPbBr_3$ nanocomposite exhibits 2–3 times more photoresponse Φ than pure zinc oxide. Thus, the sensitization effect of $CsPbBr_3$ NCs on the ZnO is revealed not only in an increase in photoconductivity, but also in an increase in photoresponse. In inert gas (Ar) atmosphere, the photoconductivity of both samples shows a weak gradual increase, while in pure oxygen atmosphere the photoconductivity of both samples decreases. The photoresponse Φ of the samples in an oxygen-free environment slightly decreases, and increases again in pure oxygen (Table 2).

The photoconductivity of the ZnO/$CsPbBr_3$ nanocomposite was measured in an Ar and O_2 atmosphere in addition under various duration periodic cycles (Fig. 8a), maintaining t_{light} = t_{dark} in each cycle. Surprisingly, it turned out that the value Φ is determined mainly by the duration of t_{dark}, both in oxygen and argon. According to the obtained data, a 5 s illumination is already sufficient to return the conductivity of the sensor to a stationary level, while in the dark the conductivity of the sensor decreases continuously. It can be concluded that the photoresponse Φ increases roughly proportional to $\sqrt{t_{dark}}$ in both Ar and O_2 atmosphere, with larger values of Φ in oxygen than in argon (Fig. 8b).

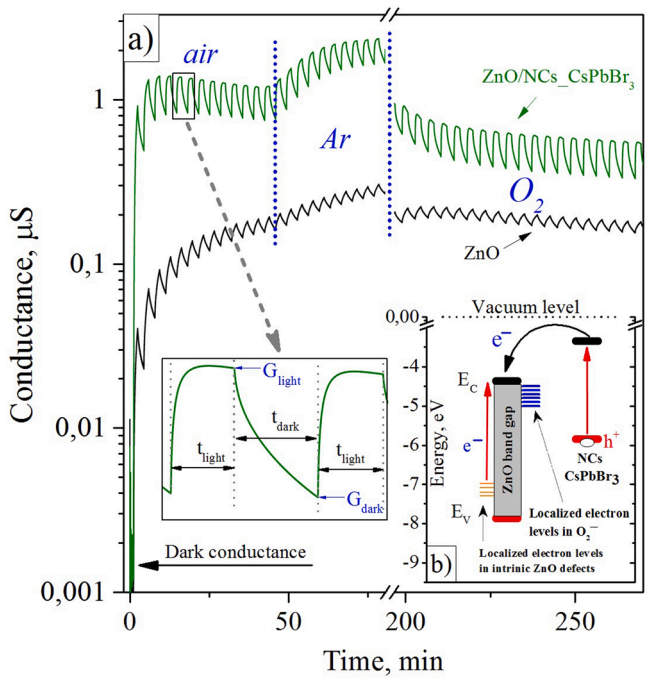

Fig. 7. (a) Photoconductivity of ZnO/$CsPbBr_3$ nanocomposite (green line) and non-sensitized ZnO (black line) under periodical (t_{dark}=t_{light} = 2 min) blue LED illumination measured at room temperature in the atmosphere of dry air, argon and oxygen gases; (b) band diagram showing photoinduced electron transfer from $CsPbBr_3$ NCs to ZnO conduction band; the relative position of energy levels in ZnO and $CsPbBr_3$ NCs are taken from [32]; near the bottom of the ZnO conduction band, the assumed position of the levels of localized electrons in chemisorbed oxygen molecules is also shown. (For interpretation of the references to colour in the Figure, the reader is referred to the web version of this article).

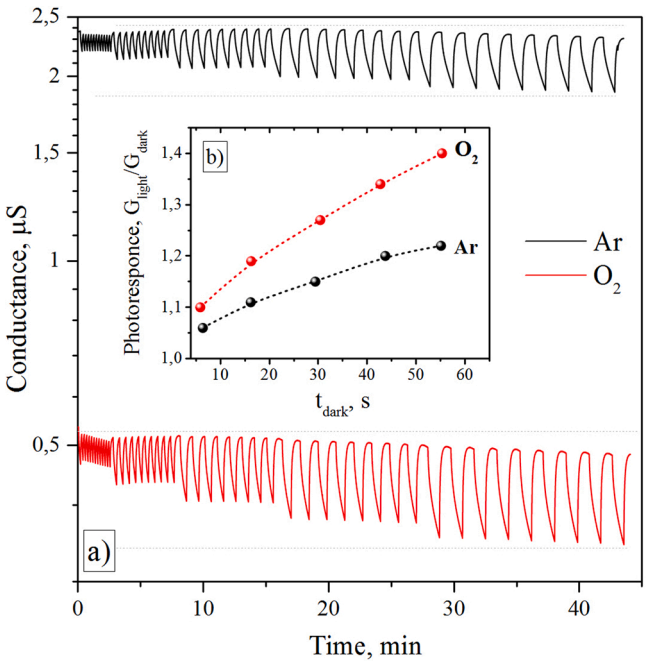

Fig. 8. a) Photoconductivity of ZnO/$CsPbBr_3$ nanocomposite under various durations (t_{dark}=t_{light} = 6÷55 s) of periodical blue LED illumination cycles measured at room temperature in the atmosphere of argon (black line) and oxygen (red line) gases; the inset shows the dependence of the photoresponse Φ on the duration of the dark period t_{dark} in argon (black line) and oxygen (red line). (For interpretation of the references to colour in the Figure, the reader is referred to the web version of this article).

Table 2
Photoresponse Φ of sensors in air, argon and oxygen atmosphere under periodic blue LED illumination at 25 °C.

Sample	air	Ar	O_2
ZnO	1.24	1.18	1.16
ZnO/$CsPbBr_3$	1.56	1.45	1.65

3.4. Light-induced sensitivity to NO_2

Our preliminary studies have shown that the ZnO/$CsPbBr_3$ nanocomposite demonstrates enhanced photoresponse for heating up to 150 °C in dry air (Supplementary Information, Fig. S9). For sensor measurements, a more sparing temperature range of up to 100 °C was chosen to avoid possible decomposition of the sensitizer during prolonged heating. Fig. 9 presents the results of *in situ* measurements of the ZnO/$CsPbBr_3$ electrical resistance (compared with the non-sensitized nanocrystalline ZnO sensor) in the presence of NO_2 in the concentration range 0.5–3.0 ppm in dry air. The measurements were carried out under periodic blue LED illumination (t_{light} = t_{dark} = 20 s) with a stepwise change of NO_2 concentration both upwards and downwards. Four cycles of measurements were carried out: at 25 °C, 50, 75 and 100 °C which made it possible to investigate the influence of slight heating on the sensor characteristics of the nanocomposite under illumination.

As can be seen from Fig. 9, in the temperature range of 25−100 °C the ZnO/$CsPbBr_3$ nanocomposite shows a principally reversible concentration-dependent response to NO_2. The non-sensitized ZnO-based sensor shows a well-distinguishable reversible photoresponse to NO_2 at 75 and 100 °C, but at lower temperatures the response to NO_2 is difficult to establish, since the resistance of ZnO is off scale (>10GΩ).

Since the adsorption of NO_2 takes place to the greatest extent under the dark conditions, the sensor signal can be calculated as a ratio between the dark resistance of the sensor in the presence of NO_2 ($R_{dark,\ NO_2}$) to the dark resistance in air ($R_{dark,\ air}$):

$$S = \frac{R_{dark,\ NO_2}}{R_{dark,\ air}} \quad (4)$$

The dependence of Φ and S on the NO_2 concentration for the ZnO/$CsPbBr_3$ nanocomposite at other temperatures is shown on Figs. 10 and 11, respectively. Two trends are clearly visible: with increasing temperature, the absolute values of Φ and S gradually decrease and the graph S(C_{NO2}) become more flat. It is interesting to note that the shape of S(C_{NO2}) graphs is determined by the direction of change in NO_2 concentration. When the concentration of NO_2 increases, the graphs are typically non-linear; when the concentration of NO_2 decreases, the graphs become almost linear on the log-log plot, which suggests the power law for the sensor signal dependence on the NO_2 concentration:

$$S \sim C_{NO_2}^{m} \quad (5)$$

The maximum value $m = 2.28$ is observed at room temperature, then with increasing temperature the slope of the curve decreases, acquiring values m of 2.00, 1.70, 1.28 at 50, 75 and 100 °C respectively. For non-sensitized ZnO at 100 °C the value of m is 1.09.

Thus, the S(C_{NO2}) and Φ(C_{NO2}) graphs show hysteresis for increasing *versus* decreasing NO_2 concentration. Measurements performed at 75 °C demonstrate the smallest hysteresis (Figs. 10c and 11c); with further heating (up to 100 °C) the area of hysteresis increases again (Fig. 10d). The dependence of the S and Φ on temperature has a different character (Fig. 12). It can be seen that the sensor signal changes with temperature more dramatically than the photoresponse. On the Arrhenius plot, the S (T) probably indicates an activation character, while the Φ(T) shows a different non-Arrhenius behavior.

Long-term stability of the ZnO/$CsPbBr_3$ nanocomposite was obtained by testing 1 ppm NO_2 during 31 days and the photoresponse decreases

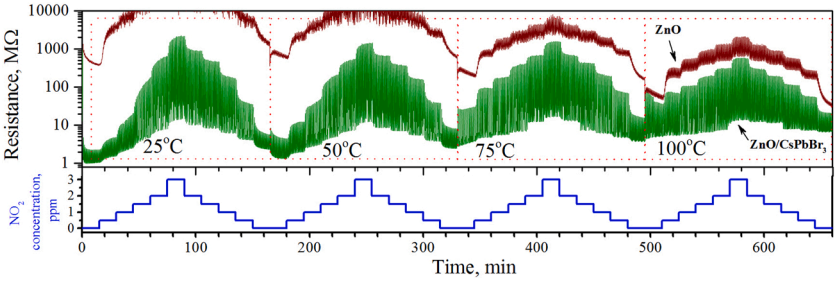

Fig. 9. Sensor measurements of ZnO/$CsPbBr_3$ nanocomposite (green line) to NO_2 under periodically blue LED illumination (t_{light}=t_{dark} = 20 s) and four temperatures: room (25 °C), 50, 75 and 100 °C. Blue line demonstrates the stepwise changing of NO_2 concentration. Red line shows the resistance of a sensor based on pure ZnO without sensitizers, which becomes electrically conductive under blue LED illumination only when heated to 75-100 °C in air. (For interpretation of the references to colour in the Figure, the reader is referred to the web version of this article).

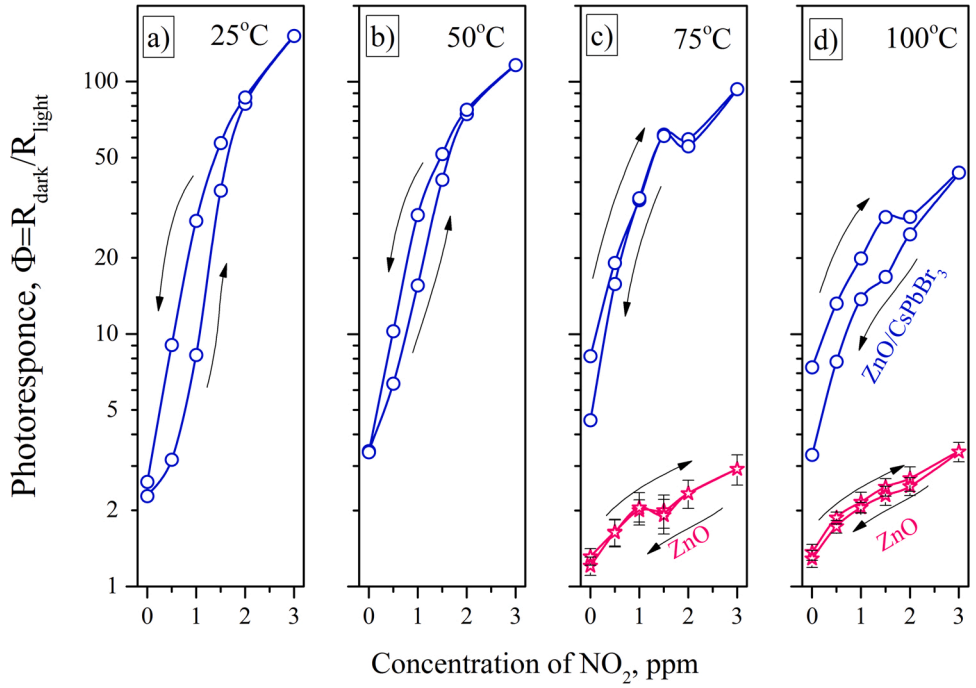

Fig. 10. Dependence of the photoresponse Φ of the ZnO/NCs_$CsPbBr_3$ nanocomposite on the concentration NO_2 at a temperature of 25 (a), 50 (b), 75 (c) and 100 °C (d). The arrows show the direction of change in NO_2 concentration.

about of 15 % during this period and reaches a plateau, which represents the reasonable long-term stability for NO_2 detection (Fig. S10, Supplementary Information).

Finally, we investigated the effect of humidity on the gas sensitivity of the ZnO/$CsPbBr_3$ nanocomposite to NO_2 at the optimal temperature of the nanocomposite layer (75 °C), by performing sensor measurements in dry air, as well as at 60 and 100 % humidity (which corresponded to an absolute water content in air of 0.014 and 0.023 g/l, respectively) (Fig. 13). In agreement with some studies [68,69], we found that humidity results in a gradual decrease in the sensor signal, however, does not have a dramatic effect. For example, at 3 ppm NO_2, an increase in air humidity from 1 to 100 % leads to a drop in the sensor signal by 38.5 %, while its absolute value remains high anyway (S = 200 at 1 % hum. *vs.* S = 123 at 100 % hum., (Fig. 14)). Thus, the ZnO/$CsPbBr_3$ nanocomposite shows superior sensor characteristics, while the presence of moisture does not interfere with reliable NO_2 detection in air. It is important that during measurements in a humid atmosphere, there was no deterioration in the sensor properties of nanocomposites, nor was a significant effect found on the reversibility of the interaction of NO_2 with ZnO/$CsPbBr_3$ nanocomposite with a successive increase and decrease in the NO_2 concentration.

Compared to existing visible-light activated resistive sensors for NO_2 detection, sensitized by low-bandgap semiconductor nanoparticles, dyes, metal nanoparticles and carbone-based materials, the sensor tested in this work shows a high response at a relatively low illuminance power (Table 3).

3.5. *Mechanism of light-induced gas sensitivity*

The gas sensitivity of semiconductor sensors under light illumination is based on two types of processes: charge carriers photogeneration and their interaction with adsorbed gas molecules. During the illumination the NCs $CsPbBr_3$ harvest visible light and photoexcited charge carriers are generated in them. There are several ways to recombine the photoexcited charge carriers: 1) radiative recombination (photoluminescence); 2) nonradiative recombination (by trapping of electrons to defect levels); 3) injection of electrons into the conduction band of the ZnO due to a suitable mutual arrangement of energy levels in oxide matrix and perovskite photosensitizer. Nonradiative recombination in $CsPbBr_3$ is suppressed due to the high defect tolerance of perovskite $CsPbBr_3$ structure [41]. The excited-state lifetime at photoluminescence is 10^{-9} - 10^{-8} s, while the injection of electrons occurs within ~10^{-12} s, so the latter process is the most probable and, as a result, leads to the separation of charge carriers between ZnO and $CsPbBr_3$ with high efficiency:

$$ZnO/CsPbBr_3 \xrightarrow{h\nu} ZnO/CsPbBr_3(e^-h^+) \rightarrow ZnO(e^-)/CsPbBr_3(h^+) \quad (6)$$

A sharp increase in the concentration of electrons in the zinc oxide

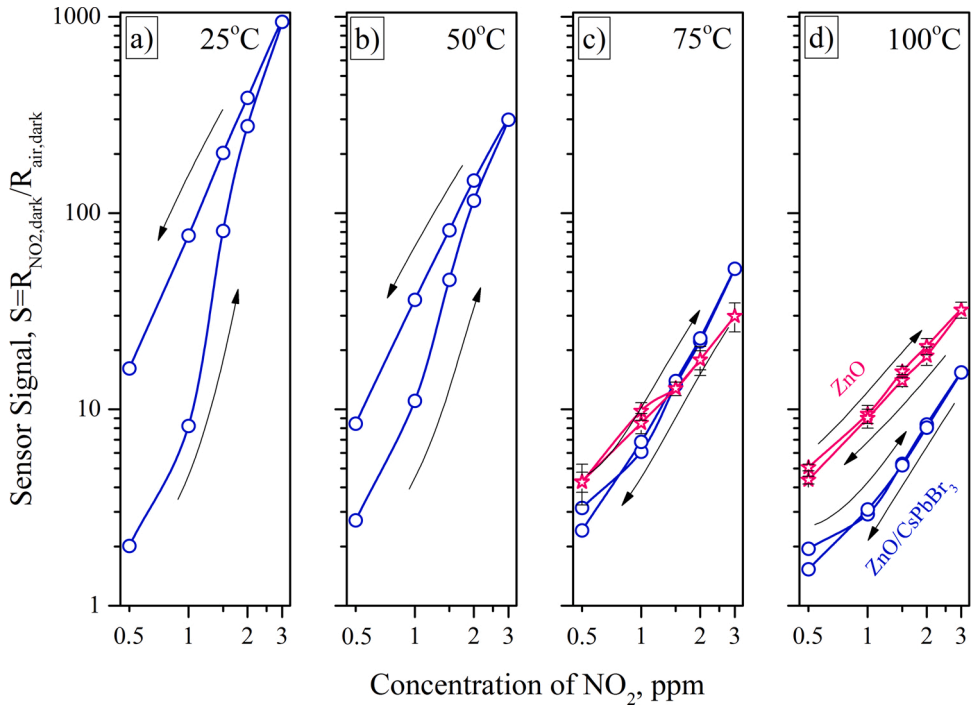

Fig. 11. Dependence of the sensor signal S of the ZnO/$CsPbBr_3$ nanocomposite on the concentration NO_2 at a temperature of 25 (a), 50 (b), 75 (c) and 100 °C (d). The arrows show the direction of change in NO_2 concentration.

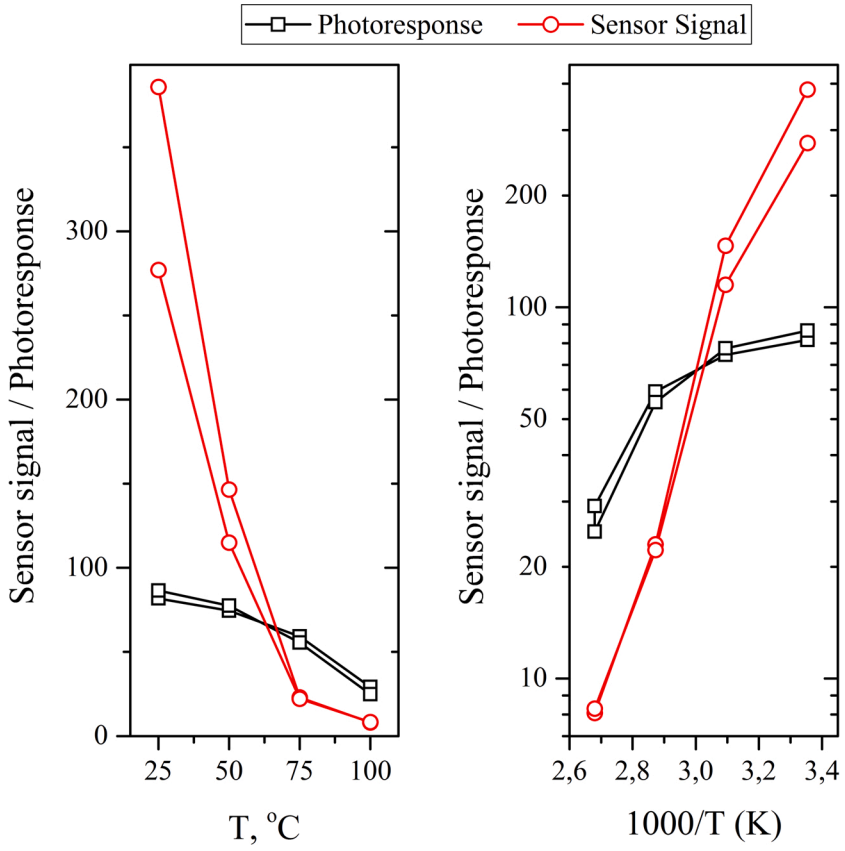

Fig. 12. Temperature dependence of sensor signal (S) and photoresponse (Φ) of ZnO/$CsPbBr_3$ nanocomposite at 2 ppm NO_2 on the linear (a) and Arrhenius (b) plots.

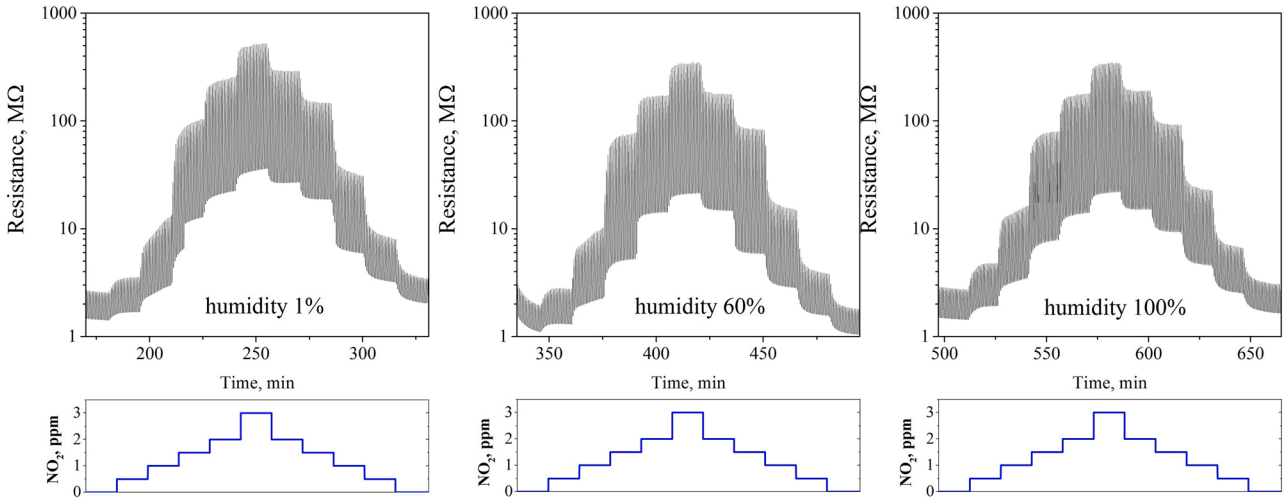

Fig. 13. Sensor measurements of ZnO/$CsPbBr_3$ nanocomposite to NO_2 at 75 °C under periodically blue LED illumination (t_{light}=t_{dark} = 20 s) and other relative hymidity (1, 60 and 100 % at 25 °C). Blue lines demonstrate the stepwise changing of NO_2 concentration during measurements. (For interpretation of the references to colour in the Figure, the reader is referred to the web version of this article).

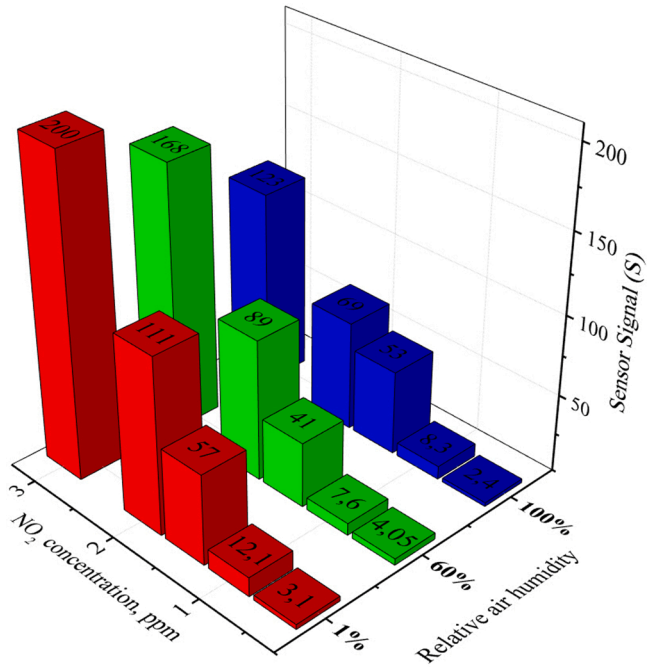

Fig. 14. Relative humidity effect on the NO_2 sensing performance of ZnO/$CsPbBr_3$ nanocomposite at operating temperature of 75 °C.

can lead to photoadsorption of oxidizing molecules on the ZnO surface:

$$O_2(ads) + e^- \rightarrow O_2(ads)^- \quad (7)$$

$$NO_2(ads) + e^- \rightarrow NO_2(ads)^- \quad (8)$$

However, the "fate" of photoexcited holes remaining in the $CsPbBr_3$ NCs is less clear. Since holes are electron acceptors, it is possible that they are involved in redox processes that contribute to the photodesorption of O_2 and NO_2 molecules:

$$O_2(ads)^- + h^+ \rightarrow O_2(ads) \quad (9)$$

$$NO_2(ads)^- + h^+ \rightarrow NO_2(ads) \text{ or} \quad (10)$$

$$NO_2(ads)^- + h^+ \rightarrow NO(ads) + O(ads) \quad (11)$$

As a result of these processes, the concentration of photoexcited charge carriers changes, which can be interpreted as an electrical (sensor) signal. Due to the significant difference in the electron affinity energy of the O_2 and NO_2 molecules (0.44 *vs.* 2.27 eV respectively), process (8) is more shifted toward the formation of a chemisorbed form than (7), which makes it possible to detect nitrogen dioxide in the presence of oxygen. Under continuous illumination, there is a dynamic equilibrium between processes (6–11), while under periodic illumination, dark and light processes can be separated from one another. In dark conditions, the photoconductivity decays due to the trapping of electrons in traps in ZnO and adsorption processes (7,8) on the ZnO surface. When illuminated, new electron-hole pairs are generated in $CsPbBr_3$ NCs, and additional electrons are pumped into the ZnO conduction band. Thus, the effect of the atmosphere on photoconductivity with periodic illumination appears in dark conditions, as was shown in measurements in oxygen and argon, so the separation of dark processes during periodic illumination improves the efficiency of NO_2 detection. At the same time, the processes (9–11) ensure the reversible operation of the sensor, preventing the accumulation of adsorbed NO_2 molecules on its surface.

A decrease in the sensor response with increasing humidity can be caused by the distraction of some part of photoexcited charge carriers into interaction with adsorbed water molecules:

$$H_2O(ads)+h^+ + 2e^- \rightarrow H_2(gas) + 1/2O_2(gas). \quad (12)$$

As a result, the processes (7)-(11) corresponding to the NO_2 gas sensitivity become less effective.

It is reasonable to compare the obtained data with the measurements that we carried out earlier on nanocomposites based on an identical nanocrystalline ZnO matrix and colloidal CdSe quantum dots (QDs) [33, 34]. Under similar conditions for NO_2 detection at room temperature, ZnO/QD_CdSe nanocomposites demonstrates substantially lower photoresponse and sensor signal than ZnO/NCs_$CsPbBr_3$ (typical values for $\Phi = 2$ *vs.* 8–30, for S = 30 *vs.* 80–200 at 1.5 ppm NO_2).

4. Conclusions

In summary, a nanocomposite consisting of nanocrystalline ZnO with wurtzite structure and colloidal $CsPbBr_3$ NCs with orthorhombic (*Pnma*) perovskite structure was synthesized in this work by chemical precipitation and high temperature colloidal synthesis. The average crystallite size was 22 ± 5.0 nm for ZnO crystallites and 15 ± 6 nm for $CsPbBr_3$ cubic-shaped NCs respectively. The structure, morphology

Table 3
Comparison of sensing performances between this work and existing ZnO-based visible-light activated NO_2 resistive sensors.

Sensing Material	Parametres of light activation		Detection conditions		Sensor Signal, R_{gas}/R_{air}	Ref
	Wavelength, nm	Irradiance, $mW^{*}cm^{-1}$	Temperature, °C	NO_2, ppm		
ZnO/N719-dye	480	370	RT (25)	1.25	1.43	[15]
ZnO/Ag	470	75	RT (25)	1	1.55	[22]
Au-ZnO nanorod array films	495	50	RT (25)	1	1.25	[23]
ZnO nanorod/Au hybrids	532	2	RT (25)	1	4.66	[24]
ZnO/Pd hybrids	475	0.8	RT (25)	1	106	[25]
ZnO/CdS	510	50	RT (25)	1	31.9	[27]
ZnO/g-C_3N_4	460	1.27	RT (27)	7	44.8	[31]
rGO@ZnO_{1-x} composite	white light	150	RT (25)	0.1	5.66	[32]
ZnO/CdSe QDs	535	20	RT (25)	0.85	20	[33]
ZnO/InP QDs	535	20	RT (25)	1	10.2	[35]
ZnO/CdS@ZnTe QDs	535	20	RT (25)	1	18	[36]
ZnO (nanorods)/PbS QDs	850	1	RT (25)	1	1.24	[37]
ZnO/$CsPbBr_3$ NCs	470	8	RT (25)	1	up to 75	This work
			75	1	6.5	

and composition of samples were confirmed by XRD, HAADF-STEM, XPS and ICP-MS. The photoconductivity and visible-light activated gas sensor properties to NO_2 were investigated in the temperature range of 25−100 °C and the air humidity from 1 to 100 %. The sensitizing effect of $CsPbBr_3$ NCs on the ZnO photoconductivity could be explain based on Marcus model of photoinduced transfer of electrons: photoexcited charge carriers appear in $CsPbBr_3$ NCs under the visible light irradiation and separate between ZnO and $CsPbBr_3$ NCs due to a suitable mutual arrangement of energy levels in the nanocrystals. According to the calculations, the photoinduced transfer of electrons from $CsPbBr_3$ NCs to ZnO is characterized by a higher constant of electron transfer rate compared CdSe and InP QDs, which ensures more efficient separation of photogenerated charge carriers. The interaction of visible-light-generated charge carriers (electrons and holes) with adsorbed gas molecules is the cause of the enhanced gas sensitivity of ZnO/$CsPbBr_3$ nanocomposite compared to pure nanocrystalline ZnO. At the same time, it was demonstrated that the gas-sensing perfomance of ZnO/$CsPbBr_3$ nanocomposite can be successfully optimized by combining of light-activation and slight heating of sensor layer in range of 25−100 °C, at that the sensor signal and photoresponse decrease with increasing temperature. It was found that the optimum temperature, providing the best reversibility of sensor measurements, was 75 °C. Although using lead halide perovskites forecasted poor stability against moisture, the ZnO/$CsPbBr_3$ nanocomposite shows good stability of the gas-sensitivity in humid air, however, a decrease in the sensor signal to NO_2 with an increase in air humidity was noted.

CRediT authorship contribution statement

A.S. Chizhov: Project administration, Funding acquisition, Investigation, Conceptualization, Methodology, Writing - original draft, Writing - review & editing, Formal analysis. **M.N. Rumyantseva:** Supervision, Methodology, Conceptualization, Resources, Writing - review & editing. **K.A. Drozdov:** Investigation, Formal analysis. **I.V. Krylov:** Investigation. **M. Batuk:** Investigation, Writing - review & editing, Formal analysis. **J. Hadermann:** Supervision, Writing - review & editing. **D.G. Filatova:** Investigation, Formal analysis. **N.O. Khmelevsky:** Investigation. **V.F. Kozlovsky:** Investigation. **L.N. Maltseva:** Investigation, Formal analysis. **A.M. Gaskov:** Resources, Conceptualization, Writing - review & editing.

Declaration of Competing Interest

The authors report no declarations of interest.

Acknowledgements

The reported study was funded by RFBR according to the research project № 18-33-01004 and in part by a grant from the St. Petersburg State University – Event 3-2018 (id: 46380300).

Element mapping for sensors were supported by M.V. Lomonosov Moscow State University Program of Development (X-ray fluorescence spectrometer Tornado M4 plus).

Appendix A. Supplementary data

Supplementary material related to this article can be found, in the online version, at doi:https://doi.org/10.1016/j.snb.2020.129035.

References

[1] N. Barsan, D. Koziej, U. Weimar, Metal oxide-based gas sensor research: How to? Sens. Actuators B Chem. 121 (1) (2007) 18–35, https://doi.org/10.1016/j.snb.2006.09.047.

[2] N. Yamazoe, G. Sakai, K. Shimanoe, Oxide semiconductor gas sensors, Catal. Surv. Asia 7 (2003) 63, https://doi.org/10.1023/A:1023436725457.

[3] A. Maricutsa, M. Rumyantseva, A. Gaskov, Selectivity of catalytically modified tin dioxide to CO and NH_3 gas mixtures, Chemosensors 3 (4) (2015) 241–252, https://doi.org/10.3390/chemosensors3040241.

[4] G. Tofighi, D. Degler, B. Junker, S. Müller, H. Lichtenberg, W. Wang, U. Weimar, N. Barsan, J.-D. Grunwaldt, Microfluidically synthesized Au, Pd and AuPd nanoparticles supported on SnO_2 for gas sensing applications, Sens. Actuators B Chem. 292 (2019) 48–56, https://doi.org/10.1016/j.snb.2019.02.107.

[5] R. Ghosh, J.W. Gardner, P.K. Guha, Air pollution monitoring using near room temperature resistive gas sensors: a review, IEEE Trans. Electron Devices 66 (8) (2019) 3254–3264, https://doi.org/10.1109/TED.2019.2924112.

[6] N. Markiewicz, O. Casals, C. Fabrega, I. Gracia, C. Cane, H.S. Wasisto, A. Waag, J. D. Prades, Micro light plates for low-power photoactivated (gas) sensors, Appl. Phys. Lett. 114 (2019), 053508, https://doi.org/10.1063/1.5078497.

[7] E. Comini, G. Faglia, G. Sberveglieri, UV light activation of tin oxide thin films for NO_2 sensing at low temperatures, Sens. Actuators B Chem. 78 (1–3) (2001) 73–77, https://doi.org/10.1016/S0925-4005(01)00796-1.

[8] S.-W. Fan, A.K. Srivastava, V.P. Dravid, UV-activated room-temperature gas sensing mechanism of polycrystalline ZnO, Appl. Phys. Lett. 95 (14) (2009), 142106, https://doi.org/10.1063/1.3243458.

[9] J. Prades, R. Jimenez-Diaz, F. Hernandez-Ramirez, S. Barth, A. Cirera, A. Romano-Rodriguez, S. Mathur, J. Morante, Equivalence between thermal and room temperature UV light-modulated responses of gas sensors based on individual SnO_2 nanowires //, Sens. Actuators B Chem. 140 (2) (2009) 337–341, https://doi.org/10.1016/j.snb.2009.04.070.

[10] C.-L. Hsu, L.-F. Chang, T.-J. Hsueh, Light-activated humidity and gas sensing by ZnO nanowires grown on LED at room temperature, Sens. Actuators B Chem. 249 (2017) 265–267, https://doi.org/10.1016/j.snb.2017.04.083.

[11] Z. Wang, K. Wang, X. Peng, Q. Geng, X. Chen, W. Dai, X. Fu, X. Wang, Comparative study of ultraviolet light and visible light on the photo-assisted conductivity and gas sensing property of TiO_2, Sens. Actuators B Chem. 248 (2017) 724–732, https://doi.org/10.1016/j.snb.2017.04.058.

[12] A.M. Gulyaev, L.V. Van, O.B. Sarach, O.B. Mukhina, Increased sensitivity and selective capacity of gas sensors based on SnO_{2-x} films exposed to light-emitting diodes, Meas. Tech. 51 (6) (2008) 694–698, https://doi.org/10.1007/s11018-008-9102-5.

[13] L. Deng, X. Ding, D. Zeng, S. Tian, H. Li, C. Xie, Visible-light activate mesoporous WO_3 sensors with enhanced formaldehyde-sensing property at room temperature, Sens. Actuators B Chem. 163 (1) (2012) 260–266, https://doi.org/10.1016/j.snb.2012.01.049.

[14] L. Han, D. Wang, J. Cui, L. Chen, T. Jiang, Y. Lin, Study on formaldehyde gas-sensing of In_2O_3-sensitized ZnO nanoflowers under visible light irradiation at room temperature, J. Mater. Chem. 22 (2012) 12915–12920, https://doi.org/10.1039/C2JM16105B.

[15] C. Zhang, J. Wang, M.-G. Olivier, M. Debliquy, Room temperature nitrogen dioxide sensors based on n719-dye sensitized amorphous zinc oxide sensors performed under visible-light illumination, Sens. Actuators B Chem. 209 (2015) 69–77, https://doi.org/10.1016/j.snb.2014.11.090.

[16] Y. Sivalingam, E. Martinelli, A. Catini, G. Magna, G. Pomarico, F. Basoli, R. Paolesse, C. Di Natale, Gas-sensitive photoconductivity of porphyrin-functionalized ZnO nanorods, J. Phys. Chem. C 116 (16) (2012) 9151–9157, https://doi.org/10.1021/jp302225u.

[17] M. Rumyantseva, A. Nasriddinov, S. Vladimirova, S. Tokarev, O. Fedorova, I. Krylov, K. Drozdov, A. Baranchikov, A. Gaskov, Photosensitive organic-inorganic hybrid materials for room temperature gas sensor applications, Nanomaterials 8 (2018) 671, https://doi.org/10.3390/nano8090671.

[18] R.-J. Wu, Y.-C. Chiu, C.-H. Wu, Y.-J. Su, Application of Au/TiO_2 WO_3 material in visible light photoreductive ozone sensors, Thin Solid Films 574 (2015) 156–161, https://doi.org/10.1016/j.tsf.2014.12.009.

[19] Y. Yao, M. Yin, J. Yan, D. Yang, S.F. Liu, Controllable synthesis of Ag/WO_3 core-shell nanospheres for light-enhanced gas sensors, Sens. Actuators B Chem. 251 (2017) 583–589, https://doi.org/10.1016/j.snb.2017.05.007.

[20] Q. Deng, S. Gao, T. Lei, Y. Ling, S. Zhang, C. Xie, Temperature and light modulation to enhance the selectivity of Pt-modified zinc oxide gas sensor, Sens. Actuators B Chem. 247 (2017) 903–915, https://doi.org/10.1016/j.snb.2017.03.107.

[21] C.-L. Hsu, Y.-H. Lin, L.-K. Wang, T.-J. Hsueh, S.-P. Chang, S.-J. Chang, Tunable UV- and visible-light photoresponse based on p-ZnO nanostructures/n-ZnO/glass peppered with Au nanoparticles, ACS Appl. Mater. Interfaces 9 (17) (2017) 14935–14944, https://doi.org/10.1021/acsami.7b03216.

[22] Q. Zhang, G. Xie, M. Xu, Y. Su, H. Tai, H. Du, Y. Jiang, Visible light-assisted room temperature gas sensing with ZnO-Ag heterostructure nanoparticles, Sens. Actuators B Chem. 259 (2018) 269–281, https://doi.org/10.1016/j.snb.2017.12.052.

[23] C. Chen, Q. Zhang, G. Xie, M. Yao, H. Pan, H. Du, H. Tai, X. Du, Y. Su, Enhancing visible light-activated NO_2 sensing properties of Au NPs decorated ZnO nanorods by localized surface plasmon resonance and oxygen vacancies, Mater. Res. Express 7 (2020), 015924, https://doi.org/10.1088/2053-1591/ab6b64.

[24] J. Wang, S. Fan, Y. Xia, C. Yang, S. Komarneni, Room-temperature gas sensors based on ZnO nanorod/Au hybrids: visible-light-modulated dual selectivity to NO_2 and NH_3, J. Hazard. Mater. 381 (2020), 120919, https://doi.org/10.1016/j.jhazmat.2019.120919.

[25] J. Wang, C. Hu, Y. Xia, S. Komarneni, Highly sensitive, fast and reversible NO_2 sensors at room-temperature utilizing nonplasmonic electrons of ZnO/Pd hybrids, Ceram. Int. 46 (2020) 8462–8468, https://doi.org/10.1016/j.ceramint.2019.12.081.

[26] B. Wu, Z. Lin, M. Sheng, S. Hou, J. Xu, Visible-light activated ZnO/CdSe heterostructure-based gas sensors with low operating temperature, Appl. Surf. Sci. 360 (2016) 652–657, https://doi.org/10.1016/j.apsusc.2015.11.037.

[27] X. Geng, C. Zhang, M. Debliquy, Cadmium sulfide activated zinc oxide coatings deposited by liquid plasma spray for room temperature nitrogen dioxide detection under visible light illumination, Ceram. Int. 42 (4) (2016) 4845–4852, https://doi.org/10.1016/j.ceramint.2015.11.170.

[28] X. Geng, Y. Luo, B. Zheng, C. Zhang, Photon assisted room-temperature hydrogen sensors using PdO loaded WO_3 nanohybrids, Int. J. Hydrogen Energy 42 (9) (2017) 6425–6434, https://doi.org/10.1016/j.ijhydene.2016.12.117.

[29] S. Shao, Y. Chen, S. Huang, F. Jiang, Y. Wang, R. Koehn, A tunable volatile organic compound sensor by using PtO_x/GQDs/TiO_2 nanocomposite thin films at room temperature under visible-light activation, RSC Adv. 7 (2017) 39859–39868, https://doi.org/10.1039/C7RA07478F.

[30] X. Geng, J. You, J. Wang, C. Zhang, Visible light assisted nitrogen dioxide sensing using tungsten oxide-graphene oxide nanocomposite sensors, Mater. Chem. Phys. 191 (Supplement C) (2017) 114–120, https://doi.org/10.1016/j.matchemphys.2017.01.046.

[31] H. Wang, J. Bai, M. Dai, K. Liu, Y. Liu, L. Zhou, F. Liu, F. Liu, Y. Gao, X. Yan, L. Geyu, Visible light activated excellent NO_2 sensing based on 2D/2D ZnO/g-C_3N_4 heterojunction composites, Sens. Actuators B Chem. 304 (2020), 127287, https://doi.org/10.1016/j.snb.2019.127287, 304.

[32] X. Geng, P. Lu, C. Zhang, D. Lahem, M.-G. Olivier, M. Debliquy, Room-temperature NO_2 gas sensors based on rGO@ZnO_{1-x} composites: Experiments and molecular dynamics simulation, Sens. Actuators B Chem. 282 (2019) 690–702, https://doi.org/10.1016/j.snb.2018.11.123.

[33] A. Chizhov, M. Rumyantseva, R. Vasiliev, D. Filatova, K. Drozdov, I. Krylov, A. Abakumov, A. Gaskov, Visible light activated room temperature gas sensors based on nanocrystalline ZnO sensitized with CdSe quantum dots, Sens. Actuators B Chem. 205 (2014) 305–312, https://doi.org/10.1016/j.snb.2014.08.091.

[34] A. Chizhov, M. Rumyantseva, R. Vasiliev, D. Filatova, K. Drozdov, I. Krylov, A. Marchevsky, O. Karakulina, A. Abakumov, A. Gaskov, Visible light activation of room temperature NO_2 gas sensors based on ZnO, SnO_2 and In_2O_3 sensitized with CdSe quantum dots, Thin Solid Films 618 (2016) 253–262, https://doi.org/10.1016/j.tsf.2016.09.029.

[35] A.S. Chizhov, N.E. Mordvinova, M.N. Rumyantsevaa, I.V. Krylov, K.A. Drozdov, X. Li, A.M. Gaskov, The effect of CdSe and InP quantum dots on the interaction of ZnO with NO_2 under visible light irradiation, Russ. J. Inorg. Chem. 63 (4) (2018) 512–518, https://doi.org/10.1134/S0036023618040071.

[36] A. Chizhov, R. Vasiliev, M. Rumyantseva, I. Krylov, K. Drozdov, M. Batuk, J. Hadermann, A. Abakumov, A. Gaskov, Light-Activated Sub-ppm NO_2Detection by Hybrid ZnO/QD Nanomaterials vs.Charge Localization in Core-Shell QD, Front. Mater. 6 (2019) 231, https://doi.org/10.3389/fmats.2019.00231.

[37] R.S. Chen, J. Wang, Y. Xia, L. Xiang, Near infrared light enhanced room-temperature NO_2 gas sensing by hierarchical ZnO nanorods functionalized with PbS quantum dots //, SensAct B Chem 255 (2018) 2538–2545, https://doi.org/10.1016/j.snb.2017.09.059.

[38] L. Protesescu, S. Yakunin, M.I. Bodnarchuk, F. Krieg, R. Caputo, C.H. Hendon, R. X. Yang, A. Walsh, M.V. Kovalenko, Nanocrystals of cesium lead halide perovskites ($CsPbBr_3$, x = Cl, Br and I): novel optoelectronic materials showing bright emission with wide color gamut, Nano Lett. 15 (6) (2015) 3692–3696, https://doi.org/10.1021/nl5048779.

[39] V.K. Ravi, G.B. Markad, A. Nag, Band edge energies and excitonic transition probabilities of colloidal $CsPbX_3$ (x = Cl, Br, I) perovskite nanocrystals, ACS Energy Lett. 1 (4) (2016) 665–671, https://doi.org/10.1021/acsenergylett.6b00337.

[40] Q.A. Akkerman, G. Raino, M.V. Kovalenko, L. Manna, Genesis, challenges and opportunities for colloidal lead halide perovskite nanocrystals, Nat. Mater. 17 (2018) 394–405, https://doi.org/10.1038/s41563-018-0018-4.

[41] J. Kang, L.-W. Wang, High defect tolerance in lead halide perovskite $CsPbBr_3$, J. Phys. Chem. Lett. 8 (2) (2017) 489–493, https://doi.org/10.1021/acs.jpclett.6b02800.

[42] H. Chen, M. Zhang, R. Bo, C. Barugkin, J. Zheng, Q. Ma, S. Huang, A.W.Y. Ho-Baillie, K.R. Catchpole, A. Tricoli, Superior self-powered room-temperature chemical sensing with light-activated inorganic halides perovskites, Small 14 (7) (2017), 1702571, https://doi.org/10.1002/smll.201702571.

[43] H. Chen, M. Zhang, X. Fu, Z. Fusco, R. Bo, B. Xing, H.T. Nguyen, C. Barugkin, J. Zheng, C.F.J. Lau, S. Huang, A.W.Y. Ho-Baillie, K.R. Catchpole, A. Tricoli, Light-activated inorganic $CsPbBr_2I$ perovskite for room-temperature self-powered chemical sensing, J. Chem. Soc. Faraday Trans. 21 (2019) 24187–24193, https://doi.org/10.1039/c9cp03059j.

[44] Y. Chen, X. Zhang, Z. Liu, Z. Zeng, H. Zhao, X. Wang, Jiaqiang Xu, Light enhanced room temperature resistive NO_2 sensor based on a gold-loaded organic–inorganic hybrid perovskite incorporating tin dioxide, Microchim. Ichnoanal. Acta 186 (1) (2019) 47, https://doi.org/10.1007/s00604-018-3155-1.

[45] S. Marc-Antoine, G. Marco, B. Sara, L. Fabiola, F. Laura, O. Emanuele, S. Paolo, Reversible, fast, and wide-range oxygen sensor based on nanostructured organometal halide perovskite, Adv. Mater. 29 (38) (2017), 1702469, https://doi.org/10.1002/adma.201702469.

[46] X. Fu, S. Jiao, N. Dong, G. Lian, T. Zhao, S. Lv, Q. Wang, Deliang Cui, A $CH_3NH_3PbI_3$ film for a room-temperature NO_2 gas sensor with quick response and high selectivity, RSC Adv. 8 (2018) 390–395, https://doi.org/10.1039/C7RA11149E.

[47] Y. Zhuang, W. Yuan, L. Qian, S. Chen, Gaoquan Shi, High-performance gas sensors based on a thiocyanate ion-doped organometal halide perovskite, Phys. Chem. Chem. Phys. 19 (2017) 12876–12881, https://doi.org/10.1039/C7CP01646H.

[48] V.X. Hien, P.D. Hoat, P.T. Hung, S. Lee, J.-H. Lee, Y.W. Heo, Room-temperature NO_2 sensor based on a hybrid nanomaterial of methylammonium tin iodide submicron spheres and tin dioxide nanowires, Scr. Mater. 188 (2020) 107–111, https://doi.org/10.1016/j.scriptamat.2020.07.022.

[49] W. Jiao, J. He, L. Zhang, Synthesis and high ammonia gas sensitivity of (CH_3NH_3)$PbBr_{3-x}I_x$ perovskite thin film at room temperature, Sens. Actuators B Chem. 309 (2020), 127786, https://doi.org/10.1016/j.snb.2020.127786.

[50] A. Nur'aini, I. Oh, Volatile organic compound gas sensors based on methylammonium lead iodide perovskite operating at room temperature, RSC Adv. Royal Soc. Chem. 10 (2020) 12982–12987, https://doi.org/10.1039/C9RA10703G.

[51] R. Zhu, Y. Zhang, H. Zhong, X. Wang, H. Xiao, Y. Chen, X. Li, High-performance room-temperature NO_2 sensors based on $CH_3NH_3PbI_3$ semiconducting films: effect of surface capping by alkyl chain on sensor performance, J. Phys. Chem. Solids 129 (2019) 270–276, https://doi.org/10.1016/j.jpcs.2019.01.020.

[52] A. Maity, A.K. Raychaudhuri, B. Ghosh, High sensitivity NH_3 gas sensor with electrical readout made on paper with perovskite halide as sensor material, Sci. Rep. 9 (2019) 7777, https://doi.org/10.1038/s41598-019-43961-6.

[53] A.D. Sheikh, V. Vhanalakar, A. Katware, K. Pawar, P.S. Patil, Two-step antisolvent precipitated MAPbI3-Pellet-Based robust room-temperature Ammonia sensor, Adv. Mater. Technol. 4 (2019) https://doi.org/1900251, 10.1002/admt.201900251.

[54] M.-Y. Zhu, L.-X. Zhang, J. Yin, J.-J. Chen, L.-J. Bie, B.D. Fahlman, Physisorption induced p-xylene gas-sensing performance of $(C_4H_9NH_3)_2PbI_4$ layered perovskite, Sens. Actuators B Chem. 282 (2019) 659–664, https://doi.org/10.1016/j.snb.2018.11.124.

[55] K. Gagaoudakis, E. Kostopoulou, A. Faka, V. Argyrou, A. Binas, V. Kiriakidis, G. Stratakis, Ligand-free all-inorganic metal halide nanocubes for fast, ultra-sensitive and self-powered ozone sensors, Nanoscale Adv. 1 (7) (2019) 2699–2706, https://doi.org/10.1039/C9NA00219G.

[56] M. Auf der Maur, A. Pecchia, G. Penazzi, W. Rodrigues, A. Di Carlo, Efficiency drop in green InGaN=GaN light emitting diodes: the role of random alloy fluctuations, Phys. Rev. Lett. 595 (116) (2016), 027401, https://doi.org/10.1103/PhysRevLett.116.027401.

[57] M. Kneissl, T. Kolbe, C. Chua, V. Kueller, N. Lobo, J. Stell-mach, A. Knauer, H. Rodriguez, S. Einfeldt, Z. Yang, N.M. Johnson, M. Weyers, Advances in group III-nitride-based deep UV light-emitting diode technology, Semicond. Sci. Technol. 26 (1) (2011), 014036, https://doi.org/10.1088/0268-1242/26/1/014036.

[58] P. Cottingham, R.L. Brutchey, On the crystal structure of colloidally prepared $CsPbBr_3$ quantum dots, Chem. Commun. 52 (2016) 5246–5249, https://doi.org/10.1039/C6CC01088A.
[59] M.C. Brennan, M. Kuno, S. Rouvimov, Crystal structure of individual $CsPbBr_3$Perovskite nanocubes, Inorg. Chem. 58 (2) (2019) 1555–1560, https://doi.org/10.1021/acs.inorgchem.8b03078.
[60] James D. McGettrick, Katherine Hooper, Adam Pockett, Jenny Baker, Joel Troughton, Matthew Carnie, Trystan Watson, Sources of Pb(0) artefacts during XPS analysis of lead halide perovskites, Mater. Lett. 251 (2019) 98–101, https://doi.org/10.1016/j.matlet.2019.04.081.
[61] K. Drozdov, V. Kochnev, A. Dobrovolsky, R. Vasiliev, A. Babynina, M. Rumyantseva, A. Gaskov, L. Ryabova, D. Khokhlov, Photoconductivity of composite structures based on porous SnO_2 sensitized with CdSe nanocrystals, Semiconductors 47 (3) (2013) 383–386, https://doi.org/10.1134/S106378261303007X.
[62] K.A. Drozdov, V.I. Kochnev, A.A. Dobrovolsky, A.V. Popelo, M.N. Rumyantseva, A. M. Gaskov, L.I. Ryabova, D.R. Khokhlov, R.B. Vasiliev, Photoconductivity of structures based on the SnO_2 porous matrix coupled with core-shell CdSe/CdS quantum dots, Appl. Phys. Lett. 103 (2013), 133115, https://doi.org/10.1063/1.4823549.
[63] R.B. Vasiliev, A.V. Babynina, O.A. Maslova, M.N. Rumyantseva, L.I. Ryabova, A. A. Dobrovolsky, K.A. Drozdov, D.R. Khokhlov, A.M. Abakumov, A.M. Gaskov, Photoconductivity of nanocrystalline SnO2 sensitized with colloidal CdSe quantum dots, J. Mater. Chem. C 1 (5) (2013) 1005–1010, https://doi.org/10.1039/C2TC00236A.
[64] K. Tvrdy, P.A. Frantsuzov, P.V. Kamat, Photoinduced electron transfer from semiconductor quantum dots to metal oxide nanoparticles, Proc. Natl. Acad. Sci. 108 (1) (2011) 29–34, https://doi.org/10.1073/pnas.1011972107.
[65] R.A. Marcus, Chemical and electrochemical electron-transfer theory, Annu. Rev. Phys. Chem. 15 (1) (1964) 155–196, https://doi.org/10.1146/annurev.pc.15.100164.001103.
[66] Ch.Y. Wang, V. Cimalla, Th. Kups, C.-C. Röhlig, Th. Stauden, O. Ambacher, Integration of In_2O_3 nanoparticle based ozone sensors with light emitting diodes, Appl. Phys. Lett. 91 (2007), 103509, https://doi.org/10.1063/1.2779971.
[67] O. Gonzalez, Tesfalem G. Welearegay, X. Vilanova, E. Llobet, Using the transient response of WO_3 nanoneedles under pulsed UV light in the detection of NH_3 and NO_2, Sensors 18 (5) (2018) 1346, https://doi.org/10.3390/s18051346.
[68] G. Lu, J. Xu, J. Sun, Y. Yu, Y. Zhang, F. Liu, UV-enhanced room temperature NO_2 sensor using ZnO nanorods modified with SnO_2 nanoparticles, Sens. Actuators B Chem. 162 (1) (2012) 82–88, https://doi.org/10.1016/j.snb.2011.12.039.
[69] T. Wang, Q. Yu, S. Zhang, X. Kou, P. Sun, G. Lu, Rational design of 3D inverse opal heterogeneous composite microspheres as excellent visible-light-induced NO_2 sensors at room temperature, Nanoscale 10 (2018) 4841, https://doi.org/10.1039/C7NR08366A.